

Minute-Scale Photonic Quantum Memory

You-Cai Lv,^{1, 2, 3, 4} Yu-Jia Zhu,^{1, 2, 3, 4} Zong-Quan Zhou,^{1, 2, 3, 4}, ^{*} Chuan-Feng Li,^{1, 2, 3, 4} and Guang-Can Guo^{1, 2, 3, 4}

¹*Laboratory of Quantum Information,*

University of Science and Technology of China, Hefei, 230026, China

²*Anhui Province Key Laboratory of Quantum Network,*

University of Science and Technology of China, Hefei 230026, China

³*CAS Center For Excellence in Quantum Information and Quantum Physics,*

University of Science and Technology of China, Hefei, 230026, China

⁴*Hefei National Laboratory, University of Science and Technology of China, Hefei 230088, China*

(Dated: November 18, 2025)

Long-lived storage of single photons is a fundamental requirement for enabling quantum communication and foundational tests of quantum physics over extended distances. While the implementation of a global-scale quantum network requires quantum storage times on the order of seconds to minutes, existing photonic quantum memories have so far been limited to subsecond lifetimes. Although $^{151}\text{Eu}^{3+}:\text{Y}_2\text{SiO}_5$ crystals exhibit substantially extended spin coherence times at the ‘magic’ magnetic field, the concomitant weak optical absorption has until now prevented single-photon storage. Here, we overcome this challenge by integrating a noiseless photon echo protocol—which makes full use of the crystal’s natural absorption for photonic storage—with a universally robust dynamical decoupling sequence incorporating adiabatic pulses to protect nuclear spin coherence, enabling long-lived quantum storage at the ‘magic’ magnetic field. At a storage time of 5.6 s, we achieve a time-bin qubit storage fidelity of $88.0 \pm 2.1\%$, surpassing the maximum fidelity attainable via classical strategies. Our device reaches a $1/e$ storage lifetime of 27.6 ± 0.6 s, enabling single-photon-level storage for 42 s with a signal-to-noise ratio greater than unity. This work establishes photonic quantum memory in the minute-scale regime, laying a solid foundation for global-scale quantum network and deep-space quantum experiments.

Quantum entanglement distribution is currently limited to 420 km in optical fibers [1] and 1200 km via a single low-Earth-orbit satellite [2]. Quantum repeaters [3, 4] provide a scalable path beyond these ranges by dividing the total communication distance into shorter elementary links, synchronized via long-lived quantum memories. Realizing a global-scale quantum network will require quantum storage times on the order of seconds to minutes [4–7]. Transportable quantum memories further broaden this vision by enabling worldwide quantum communication via the physical transport of stored quantum states, with target storage times approaching one hour [8, 9]. Similarly, foundational experiments with deep-space quantum links—such as Bell tests over astronomical baselines and studies of entanglement dynamics in gravitational fields—also require photonic storage times lasting seconds to minutes [10–12].

However, existing photonic quantum memories remain limited to subsecond storage times [13–16]. The current state of the art reaches a $1/e$ lifetime of approximately 0.1 s for absorptive-type quantum memories [13, 14] and 0.46 s for emissive-type systems [16], falling substantially short of the demands for global-scale quantum networks or advanced memory-assisted applications discussed above.

$\text{Eu}^{3+}:\text{Y}_2\text{SiO}_5$ crystals are a leading candidate for long-lived photonic quantum memory [14, 17–19], having demonstrated 1-hour storage of classical light at a ‘magic’

magnetic field featuring zero first-order Zeeman (ZEFOZ) effects [20]. Yet, the single-photon storage time remains confined to 0.1 s, achieved at near-zero field to ensure sufficient optical absorption [14]. This is because operating at the ZEFOZ magnetic field, while beneficial for spin coherence, significantly reduces optical absorption due to the complete lifting of level degeneracy. Consequently, the feasibility of long-lived quantum storage at the ZEFOZ magnetic field remains an open question [21].

In this work, we demonstrate a minute-scale photonic quantum memory by implementing the noiseless photon echo (NLPE) protocol [22] combined with a universally robust (UR) dynamical decoupling sequence [23] in $^{151}\text{Eu}^{3+}:\text{Y}_2\text{SiO}_5$ crystals under a ZEFOZ magnetic field [17]. The memory achieves a $1/e$ storage lifetime of 27.6 s—more than two orders of magnitude beyond previous records for absorptive photonic quantum memories [13, 14]. At a storage time of 5.6 s, it maintains an efficiency of 8.2% and delivers a qubit storage fidelity of $88.0 \pm 2.1\%$, unambiguously surpassing the classical bound.

Fig. 1 illustrates the experimental layout. The 580-nm laser is a frequency-doubled semiconductor laser (Top-Optica, TA-SHG) with a stabilized linewidth of approximately 1 kHz. Both the signal beam and the control beam are generated with double-passed acousto-optic modulators (AOMs). The control beam intersects the signal beam on the crystal at an angle of 1.5° , with full width at half maximum (FWHM) of 250 μm and 100 μm for the control and signal beams, respectively. Both beams travel along the b-axis of the memory crystal (MC) with the polarization aligned to the D_1 -axis. The MC is a 0.01% $^{151}\text{Eu}^{3+}:\text{Y}_2\text{SiO}_5$ crystal with a size of

* zq_zhou@ustc.edu.cn

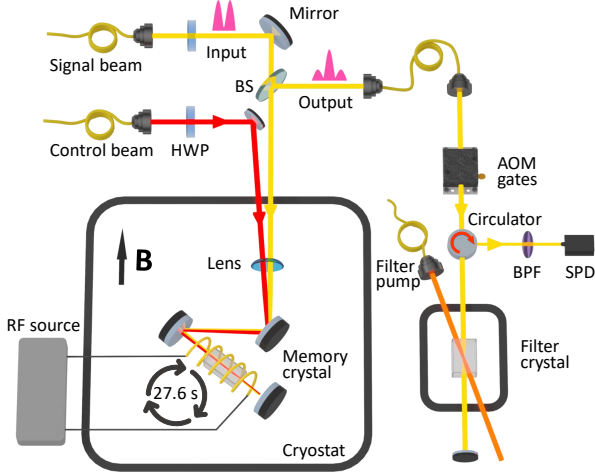


FIG. 1. Schematic of the experimental setup. The polarization of signal and control beams are controlled with half-wave plates (HWPs), to be polarized parallel to the D_1 axis of the memory crystal (MC) to maximize interaction strength. Both beams overlap inside the MC an angle of 1.5° . The signal beam propagates along the MC's b-axis, guided by three steering mirrors, and is retro-reflected along the same path. A 95(R):5(T) beam splitter (BS) separates the output signal, which is then coupled into a single-mode fiber. The MC is precisely aligned inside the magnet using two goniometer stages. Dynamical decoupling on the spin transitions is implemented by applying amplified RF pulses via solenoid coils surrounding the MC. Photonic time-bin encoded qubits are stored inside the MC with a $1/e$ lifetime of 27.6 s. The readout signal subsequently passes through a temporal gate based acousto-optic modulator (AOM), followed by spectral filtering with a double-passed filter crystal (FC) and a 0.5-nm band-pass filter (BPF). The FC is prepared by a pump beam to create a 0.8-MHz transparent spectral window centered at the signal frequency. The filtered signal is finally detected with a fiber-coupled single-photon detector (SPD).

$5 \times 4 \times 10$ mm 3 along the $D_1 \times D_2 \times b$. A solenoid coil with a diameter of 10 mm and a length of 18 mm surrounding the MC supplies the RF field for spin manipulation. The MC is cooled to 1.65 K using a low-vibration close-cycle cryostat (Attodry 2100). After the double-passed MC, the read-out pulse is temporally gated by AOMs and spectrally filtered by a double-passed filter crystal (FC) housed in a separate homemade cryostat. The FC is a 15-mm-long $^{151}\text{Eu}^{3+}:\text{Y}_2\text{SiO}_5$ crystal with a dopant concentration of 0.1%. It is prepared with a 0.8-MHz-wide transparency window at the signal frequency, outside of which the absorption depth reaches 6.6.

In order to extend the spin coherence lifetime, the memory was operated at a ZEFOZ magnetic field of 1.2968 ± 0.0002 T, applied along the direction [-0.544, -0.601, 0.586] in the crystal's $D_1 \times D_2 \times b$ coordinate frame [17, 20]. We note that the reported field strength has now been calibrated with an NMR teslameter (Metrolab, PT2026), thus representing an accurate value. The orientation of the MC is finely adjusted using two goniometer stages [20] to maximize the measured two-pulse spin coherence lifetime. After systematic optimization of the field magnitude and orientation, a two-pulse spin-echo coherence lifetime of $T_2 = 17.7 \pm 0.4$ s (Fig. 2c) was achieved for the ZEFOZ transition between states $|3\rangle_g$ and $|4\rangle_g$. The spin coherence time reported here is shorter than those achieved with shorter crystals [17, 20], owing to the compromise in magnetic field homogeneity imposed by the 10-mm interaction length—necessary for efficient single-photon absorption—which in turn decreases the effective T_2 [24]. Employing a magnet with improved homogeneity would permit longer quantum storage times, as the two-pulse spin echo T_2 can be extended to approximately 50 s.

The application of a ZEFOZ magnetic field to $^{151}\text{Eu}^{3+}:\text{Y}_2\text{SiO}_5$ lifts all level degeneracies—including hyperfine doublets and magnetically inequivalent subsites—and consequently leads to a sharp reduction in optical absorption, measured here at approximately 1 cm $^{-1}$ for the double-passed MC. In this regime, standard quantum memory protocols that depend on spectral tailoring [25, 26] to achieve atomic rephasing in an inhomogeneously broadened ensemble would suffer severe efficiency losses. We therefore adopt the NLPE protocol, which performs direct optical rephasing to make full use of the natural sample absorption for efficient quantum storage [22, 27–29].

We first calculate the energy level structure of $^{151}\text{Eu}^{3+}$ in Y_2SiO_5 crystal under the ZEFOZ magnetic field, as illustrated in Fig. 2a. The optical transition probabilities are listed in Tab. I which are calculated according to the hyperfine Hamiltonian of the ground and excited states provided in Ref. [30]. Implementation of NLPE protocol requires a four-level system whose two ground states are fixed to the ZEFOZ hyperfine transition $|3\rangle_g \leftrightarrow |4\rangle_g$. Among the optical transitions satisfying this constraint, the $|3\rangle_g \leftrightarrow |3\rangle_e$ line, which provides the highest transition strength, is selected as the signal transition. For the auxiliary excited state, we choose $|2\rangle_e$ because its transition to $|3\rangle_g$ is strong, while the $|4\rangle_g \leftrightarrow |2\rangle_e$ transition is weak; this asymmetry helps to suppress spontaneous-emission noise from the fully populated $|2\rangle_e$ level during the NLPE sequence [22].

	$ 1\rangle_e$	$ 2\rangle_e$	$ 3\rangle_e$	$ 4\rangle_e$	$ 5\rangle_e$	$ 6\rangle_e$
$ 1\rangle_g$	0.57	0.18	0.12	0.10	0.01	0.02
$ 2\rangle_g$	0.32	0.54	0.01	0.06	0.00	0.07
$ 3\rangle_g$	0.06	0.18	0.44	0.10	0.01	0.21
$ 4\rangle_g$	0.00	0.10	0.14	0.42	0.04	0.30
$ 5\rangle_g$	0.04	0.00	0.23	0.27	0.08	0.38
$ 6\rangle_g$	0.01	0.00	0.06	0.05	0.86	0.02

TABLE I. Branching ratio of optical transitions. Matrix representation of transition branching ratios between ground (columns) and excited (rows) states. Energy levels involved in the NLPE memory protocol are highlighted in red.

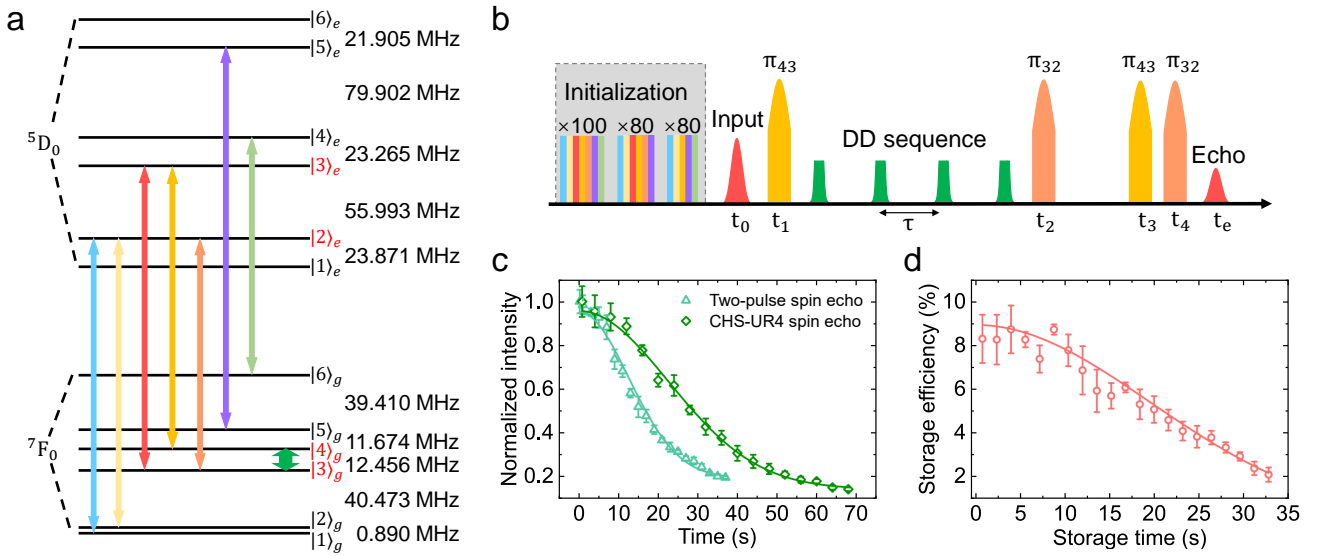


FIG. 2. Characterization of the long-lived quantum memory. **a.** Energy level structure of $^{151}\text{Eu}^{3+}$ in Y_2SiO_5 crystal under the ZEFOZ magnetic field of 1.2968(2) T. Colored lines represent optical and RF transitions: red for the signal beam, orange and coral for control beams; the green marker indicates the ZEFOZ spin transition at 12.456 MHz. **b.** Experimental sequence of the long-lived quantum memory. The gray region indicates initialization, followed by the NLPE-DD storage sequence. The final echo is emitted at $t_e = t_4 + t_3 - t_2 - t_1 + t_0$. **c.** Decay of spin echo intensity with total evolution time for two-pulse spin echo (triangle) and the CHS-UR4 sequences (diamond), fitted to $e^{-(t/T_2)^2}$. **d.** Optical storage efficiency of the NLPE-DD memory as a function of storage time, fitted to $e^{-(t/T_M)^2}$. Error bars denote ± 1 standard deviation throughout.

Fig. 2b sketches the time sequence of our long-lived photonic quantum memory. Initialization proceeds in three steps. First, a class-cleaning sequence [22, 31] selects a class of ions within a 3 MHz bandwidth. Second, spin polarization [22, 31] transfers all these ions to $|6\rangle_g$. Finally, five chirped pulses (0.8 MHz bandwidth) centered at f_{12} , f_{22} , f_{43} , f_{55} , and f_{64} back-pump the ions into the target state $|3\rangle_g$, where f_{ij} represents the transition frequency for $|i\rangle_g \leftrightarrow |j\rangle_e$. Following the initialization sequence, we obtain an absorption feature centered on the $|3\rangle_g \leftrightarrow |3\rangle_e$ transition, with a width of 0.8 MHz, a depth of 1.0, and located within a 3 MHz transparency window.

The input signal, centered at frequency f_{33} and injected at time t_0 , is a truncated Gaussian pulse with a total duration of 3 μs and a FWHM of 1.5 μs . The NLPE protocol requires four optical π pulses to perform direct optical rephasing in the inhomogeneously broadened ensemble. To this end, we implement four adiabatic complex-hyperbolic-secant (CHS) pulses [22, 32], which enable efficient and uniform π rotations across the entire ensemble. The first π_{43} pulse maps the optical signal onto the spin coherence between states $|3\rangle_g \leftrightarrow |4\rangle_g$. A subsequent π_{32} pulse converts this spin coherence into an optical coherence between $|2\rangle_e \leftrightarrow |4\rangle_g$. A second pair of π_{43} and π_{32} pulses then retrieves the optical echo signal at frequency f_{33} [28]. Since all population is eventually returned to the ground states and fluorescence from $|2\rangle_e$ is spectrally distinct from the signal, the final echo is emitted free from noise in principle. Here, π_{mn} denotes a π

pulse driving the transition $|m\rangle_g \leftrightarrow |n\rangle_e$.

Extending the spin-wave storage lifetime for arbitrary photonic states requires a robust dynamical decoupling (DD) sequence that is insensitive to the initial state. We implement a UR4 DD sequence [23], replacing all rectangular π -pulses with adiabatic CHS RF pulses [32, 33], each with a duration of 3.9 ms, a bandwidth of 22 kHz, and a peak power of 150 W. Since the precise spacing between CHS pulses directly sets the effective phase relation in the UR4 sequence (see detailed analysis in the Supplementary Information), we use a Rb-clock as the master time reference for pulse generation. This CHS-UR4 hybrid achieves optimal transfer efficiency while minimizing pulse-error-induced noise, extending the spin coherence time to $T_2 = 31.8 \pm 0.8$ s (Fig. 2c). Then we combine the NLPE memory with DD by applying the CHS-UR4 sequence after the first optical π_{43} pulse, achieving a $1/e$ quantum storage lifetime of $T_M = 27.6 \pm 0.6$ s for the NLPE-DD memory (Fig. 2d). The observed minor reduction relative to the spin coherence lifetime results from RF-induced heating, which slightly degrades optical coherence and storage efficiency.

Fig. 3a displays the photon counting histogram for the NLPE memory using weak coherent input pulses with a mean photon number of $\mu = 1.18$ per pulse. With a detection window of 2.1 μs , we obtain a storage efficiency of 9.65% and a noise level of $0.17 \pm 0.07\%$, yielding a signal-to-noise ratio (SNR) of 65.2 ± 27.2 at a storage time of 28.1 μs . Fig. 3b shows the corresponding histogram for the NLPE-DD memory under the same input

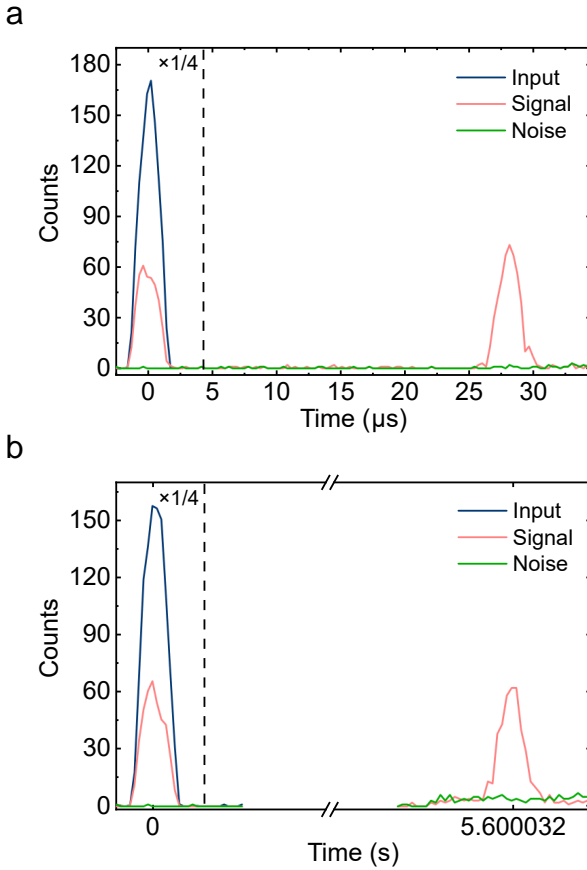


FIG. 3. Storage of single-photon level inputs. **a** and **b**. Photon counting histogram of NLPE memory (a) and NLPE-DD memory (b), measured using weak coherent input pulses with a mean photon number $\mu = 1.18$ and integrated over 35,000 experimental trials. The blue, red, and green curves denote the input photon counts, output signal, and noise level (measured without input), respectively. For clarity, data to the left of the dashed line are scaled down by a factor of 4. The shaded region indicates the 2.1 μ s detection window, yields SNRs of 65.2(27.2) and 11.3(2.5) at readout times of 28.1 μ s and 5.600032 s, respectively.

conditions, using a DD pulse interval of $\tau = 1.4$ s. At a readout time of 5.600032 s, the storage efficiency is $8.2 \pm 0.5\%$, with a SNR of 11.3 ± 2.5 . Although the NLPE-DD memory maintains an efficiency comparable to that of the NLPE memory—reflecting the high rephasing efficiency of the CHS-UR4 sequence—the observed reduction in SNR stems from an increase in noise. This increased noise originates from imperfections in the CHS-UR4 sequence across the large ensemble, which leave residual population in the $|4\rangle_g$ after DD. This residual population is subsequently excited to $|3\rangle_e$ by the second π_{43} pulse, leading to spontaneous emission noise. Despite this, the SNR achieved here is comparable to those of quantum memories incorporating DD at zero or low magnetic fields [14, 29], while extending the storage time by more than two orders of magnitude.

To demonstrate that our device indeed works in the quantum regime, we encode the inputs with time-bin qubits [22, 34]. The four input qubit states are $|e\rangle$, $|l\rangle$, $|e\rangle + |l\rangle$ and $|e\rangle + i|l\rangle$, where $|e\rangle$ and $|l\rangle$ correspond to the early and late time bins, respectively. Each pulse retains identical parameters to those used in earlier tests, with a fixed separation of 3 μ s between $|e\rangle$ and $|l\rangle$. The eigen states $|e\rangle$ and $|l\rangle$ can be directly analyzed with standard NLPE-DD sequence. To analyze the superposition states, we split the second optical π_{32} pulse into two $\pi/2$ pulses separated by 3 μ s, to read out the signal twice to effectively mimic the function of unbalanced Mach-Zehnder interferometer [22]. By tuning the phase between the two $\pi/2$ pulses, we modulate the interference of outputs to accomplish the analysis of the superposition states. The average photon number per qubit (μ_q) is 1.16. Photon counting histograms for the four input qubits are presented in Fig. 4 with a storage time of 5.600032 s.

We denote the fidelity of input qubit $|i\rangle$ as $F_{|i\rangle}$. The total fidelity is computed as $F_t = \frac{1}{3} \frac{F_{|e\rangle} + F_{|l\rangle}}{2} + \frac{2}{3} \frac{F_{|e\rangle+|l\rangle} + F_{|e\rangle+i|l\rangle}}{2}$. Here, the basis-state fidelities $F_{|e\rangle}$ and $F_{|l\rangle}$ are calculated as $\frac{S+N}{S+2N}$, where S represents the signal counts (noise excluded) and N denotes the noise counts. Specifically for $F_{|e\rangle}$, $S+N$ and N correspond, respectively, to the measured counts in the target time bin $|e\rangle$ and the counts in the orthogonal time bin $|l\rangle$. The superposition-state fidelities $F_{|e\rangle+|l\rangle}$ and $F_{|e\rangle+i|l\rangle}$ are evaluated as $\frac{V+1}{2}$, where $V = \frac{c_{max}-c_{min}}{c_{max}+c_{min}}$ is the interference visibility, with c_{max} and c_{min} representing the photon counts in the central time bin under constructive and destructive interference conditions, respectively. The measured storage fidelities are provided in Fig. 4, which give a F_t of $88.0 \pm 2.1\%$. We calculate the maximal storage fidelity that can be achieved using classical prepare-and-measure strategy which takes into account the finite storage efficiency and the Poisson statistics of input coherent states [34, 35]. The green dashed line in Fig. 4d represents this classical fidelity bound while the red solid line represents the expected storage fidelity of our device calculated according to the storage efficiency and measured noise. The measured fidelity F_t at 5.600032 s violates the classical bound (82.3%) by 2.7 standard deviations, unambiguously demonstrating this device operating in the true quantum regime. The cross over between these two lines indicates that our device operating beyond the classical limit with a minimal μ_q of 0.41.

The fundamental fidelity limit for a quantum memory using true single-photon (Fock-state) inputs is $2/3$ [36], equivalently requiring an SNR of 1:1. To probe the fundamental performance limits of our device, we extended the storage time to 42.000032 s by adjusting the CHS-UR4 pulse spacing to $\tau = 10.5$ s (Fig. 5). To reduce integration time, measurements were conducted using an input of $\mu = 4.16$ photons per pulse. The measured SNR of 5.3 corresponds to a single-photon-equivalent SNR of 1.27:1, which remains above the operational thresh-

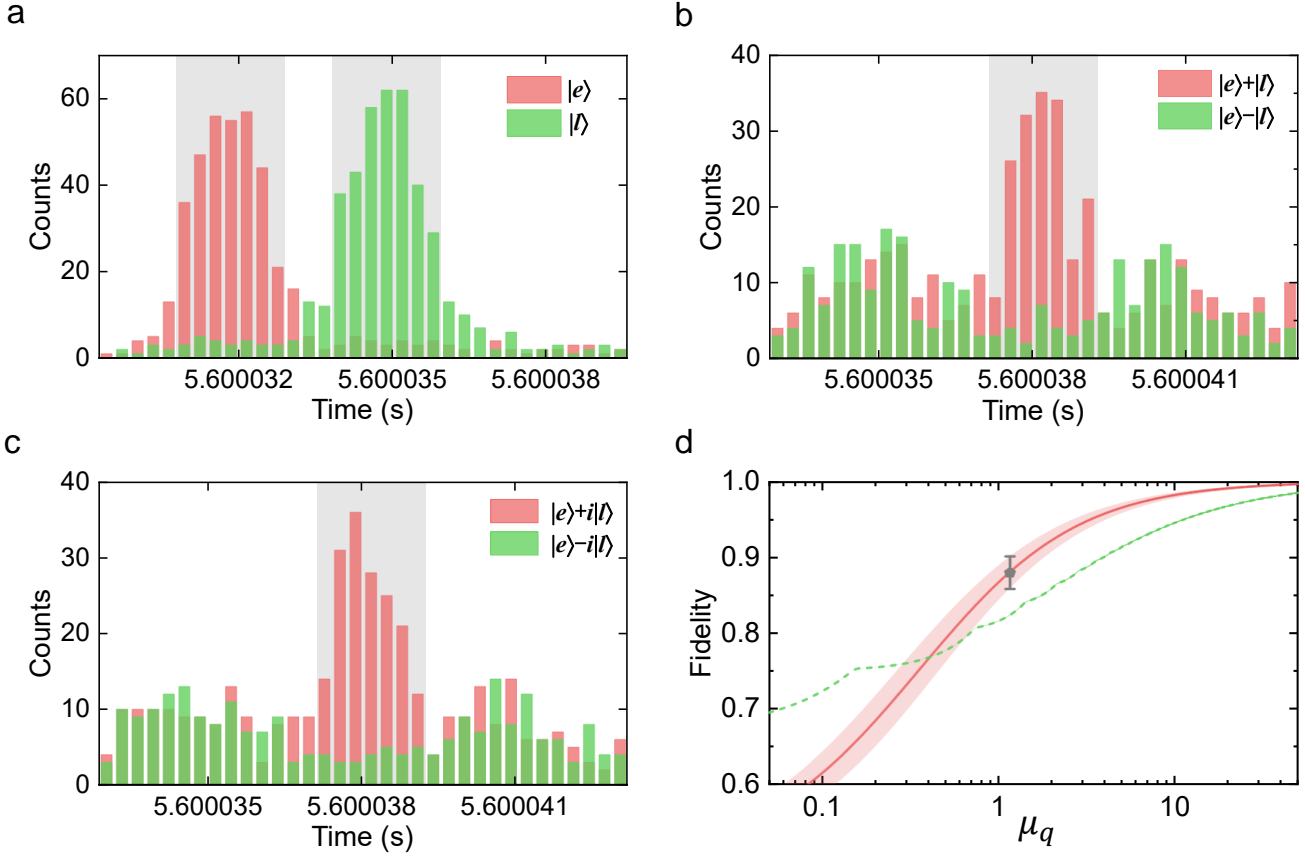


FIG. 4. **Storage of time-bin qubits for 5.600032 s.** **a.** Photon counting histogram for the input qubits $|e\rangle$ and $|l\rangle$. Output counts for $|e\rangle$ and $|l\rangle$ are shown as red and green bars, respectively. The gray-shaded region marks the 2.1 μ s detection window. The mean input photon number per qubit is $\mu_q = 1.16$, integrated over 35,000 experimental trials. The measured fidelities are $F_{|e\rangle} = 92.7 \pm 1.4\%$ and $F_{|l\rangle} = 92.7 \pm 1.4\%$. **b,c.** Photon counting histogram for the input qubit $|e\rangle + |l\rangle$ and $|e\rangle + i|l\rangle$, respectively. red and green bars correspond to constructive and destructive interference measurements for each qubit. All other experimental settings match those in **a**. The measured fidelities are $F_{|e\rangle + |l\rangle} = 85.8 \pm 2.5\%$ and $F_{|e\rangle + i|l\rangle} = 85.6 \pm 2.5\%$. **d.** Classical fidelity limit for memory as a function of μ_q . The green dashed line indicates the classical bound for a measure-and-prepare strategy under 8.2% storage efficiency. The gray dot marks the measured memory fidelity of $88.0 \pm 2.1\%$ at $\mu_q = 1.16$. The solid red line represents the expected fidelity calculated from the experimental efficiency and noise.

old for a quantum memory operating with ideal single-photon inputs. The reduction in SNR at longer storage times results from the exponential decay in storage efficiency (Fig. 2d), while the noise floor remains unchanged. This noise stability arises because the dominant noise source—residual population induced by the DD sequence—depends only on the number of RF pulses applied. Addressing the efficiency-noise trade-off in longer DD sequences will be pivotal to unlocking further gains in performance.

By implementing an NLPE-DD protocol in a $^{151}\text{Eu}^{3+}:\text{Y}_2\text{SiO}_5$ crystal at a ZEFOZ magnetic field, we have realized a photonic quantum memory with a $1/e$ lifetime of $T_M = 27.6 \pm 0.6$ s. The memory preserves photonic time-bin qubits beyond the classical fidelity limit after 5.6 s of storage—marking a 280-fold improvement over prior long-lived absorptive quantum memories [14] and fulfilling a key requirement for global-scale quantum repeater networks [5–7] and fundamental physical tests

with deep-space quantum links [10, 11].

Further extending the storage lifetime is essential for applications such as transportable quantum memories [8, 9] and quantum communication across interplanetary or inter-spacecraft links [12]. A storage time of several minutes can be straightforwardly achieved using a magnet with improved field homogeneity [24]. Substantially longer coherence can be attained by using $^{153}\text{Eu}^{3+}$ ions, which are expected to exhibit extended two-pulse spin echo T_2 due to their smaller magnetic g -tensor and reduced sensitivity to magnetic noise. Additional gains are feasible through the optimization of DD sequences with more pulses and the growth of higher-quality crystals [24]. Furthermore, near-unity storage efficiency could be reached by coupling the memory to an impedance-matched optical cavity [18], fully overcoming the weak-absorption constraint.

These advances position $^{151}\text{Eu}^{3+}:\text{Y}_2\text{SiO}_5$ crystals operating at ZEFOZ magnetic fields as the foundational hard-

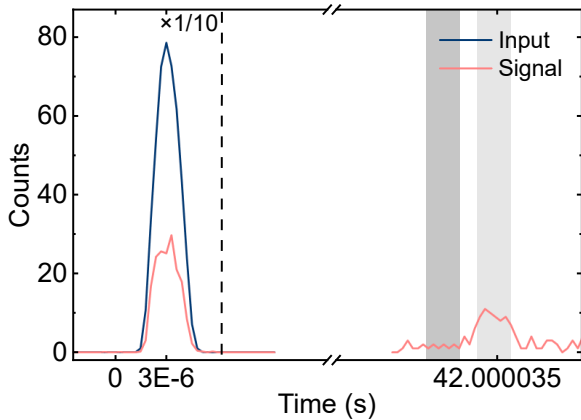


FIG. 5. **Storage of qubit $|l\rangle$ for 42.00032 s.** Photon counting histogram of the input qubit $|l\rangle$ measured using weak coherent pulses with a mean photon number $\mu = 4.16$, accumulated over 11,000 experimental trials. The blue curve indicates the input photon counts, and the red curve shows the storage process. For visual clarity, photon counts to the left of the vertical dashed line are scaled down by a factor of 10. The dark and light shaded regions mark the detection windows for the orthogonal time bin $|e\rangle$ and target time bin $|l\rangle$, respectively.

[1] Zhuang, S.-C. *et al.* Ultrabright entanglement based quantum key distribution over a 404 km optical fiber. *Phys. Rev. Lett.* **134**, 230801 (2025).

[2] Yin, J. *et al.* Satellite-based entanglement distribution over 1200 kilometers. *Science* **356**, 1140–1144 (2017).

[3] Briegel, H.-J., Dür, W., Cirac, J. I. & Zoller, P. Quantum repeaters: The role of imperfect local operations in quantum communication. *Phys. Rev. Lett.* **81**, 5932–5935 (1998).

[4] Sangouard, N., Simon, C., de Riedmatten, H. & Gisin, N. Quantum repeaters based on atomic ensembles and linear optics. *Rev. Mod. Phys.* **83**, 33–80 (2011).

[5] Gündoğan, M. *et al.* Proposal for space-borne quantum memories for global quantum networking. *npj Quantum Information* **7**, 128 (2021).

[6] Liu, P.-X., Lin, Y.-P., Zhou, Z.-Q., Li, C.-F. & Guo, G.-C. Global-scale quantum networking using hybrid-channel quantum repeaters with relays based on a chain of balloons. *arXiv:2507.15178 [quant-ph]* (2025).

[7] Tubío, V. D., Aldecocea, M., van Dam, J., Sørensen, A. & Borregaard, J. Satellite-assisted quantum communication with single photon sources and atomic memories. *arXiv:2411.09533 [quant-ph]* (2024).

[8] Gündoğan, M., Sidhu, J. S., Krutzik, M. & Oi, D. K. L. Time-delayed single satellite quantum repeater node for global quantum communications. *Optica Quantum* **2**, 140–147 (2024).

[9] Bland-Hawthorn, J., Sellars, M. J. & Bartholomew, J. G. Quantum memories and the double-slit experiment: implications for astronomical interferometry. *J. Opt. Soc. Am. B* **38**, A86–A98 (2021).

[10] Mol, J.-M. *et al.* Quantum memories for fundamental science in space. *Quantum Science and Technology* **8**, 024006 (2023).

[11] Barzel, R., Gündoğan, M., Krutzik, M., Rätzel, D. & Lämmerzahl, C. Entanglement dynamics of photon pairs and quantum memories in the gravitational field of the earth. *Quantum* **8**, 1273 (2024).

[12] Mohageg, M. *et al.* The deep space quantum link: prospective fundamental physics experiments using long-baseline quantum optics. *EPJ Quantum Technology* **9**, 25 (2022).

[13] Körber, M. *et al.* Decoherence-protected memory for a single-photon qubit. *Nat. Photon.* **12**, 18–21 (2018).

[14] Ortú, A., Holzapfel, A., Etesse, J. & Afzelius, M. Storage of photonic time-bin qubits for up to 20 ms in a rare-earth doped crystal. *npj Quantum Information* **8**, 29 (2022).

[15] Yang, S.-J., Wang, X.-J., Bao, X.-H. & Pan, J.-W. An efficient quantum light–matter interface with sub-second lifetime. *Nat. Photon.* **10**, 381–384 (2016).

[16] Wang, X.-J. *et al.* Cavity-enhanced atom-photon entanglement with subsecond lifetime. *Phys. Rev. Lett.* **126**, 090501 (2021).

[17] Zhong, M. *et al.* Optically addressable nuclear spins in a solid with a six-hour coherence time. *Nature* **517**, 177–180 (2015).

[18] Meng, R.-R. *et al.* Efficient integrated quantum memory for light. *arXiv:2511.05928 [quant-ph]* (2025).

[19] Zhu, T.-X. *et al.* A metropolitan-scale multiplexed quantum repeater with bell nonlocality. *arXiv:2508.17940 [quant-ph]* (2025).

[20] Ma, Y., Ma, Y.-Z., Zhou, Z.-Q., Li, C.-F. & Guo, G.-C. One-hour coherent optical storage in an atomic frequency comb memory. *Nat. Commun.* **12**, 2381 (2021).

[21] Afzelius, M., Gisin, N. & de Riedmatten, H. Quantum memory for photons. *Physics Today* **68**, 42 (2015).

ware for large-scale quantum repeater networks whose transportable memories serve as mobile nodes, ushering in a flexible quantum architecture that mirrors today's classical telecom infrastructure.

[22] Ma, Y.-Z. *et al.* Elimination of noise in optically rephased photon echoes. *Nat. Commun.* **12**, 4378 (2021).

[23] Genov, G. T., Schraft, D., Vitanov, N. V. & Halfmann, T. Arbitrarily accurate pulse sequences for robust dynamical decoupling. *Phys. Rev. Lett.* **118**, 133202 (2017).

[24] Ma, Y.-Z. *et al.* Monte Carlo simulation of the nuclear spin decoherence process in Eu³⁺:Y₂SiO₅ crystals. *Phys. Rev. B* **107**, 014310 (2023).

[25] de Riedmatten, H., Afzelius, M., Staudt, M. U., Simon, C. & Gisin, N. A solid-state light–matter interface at the single-photon level. *Nature* **456**, 773–777 (2008).

[26] Hedges, M. P., Longdell, J. J., Li, Y. & Sellars, M. J. Efficient quantum memory for light. *Nature* **465**, 1052–1056 (2010).

[27] Jin, M., Ma, Y.-Z., Zhou, Z.-Q., Li, C.-F. & Guo, G.-C. A faithful solid-state spin-wave quantum memory for polarization qubits. *Science Bulletin* **67**, 676–678 (2022).

[28] Zhu, T.-X. *et al.* Integrated spin-wave quantum memory. *Nat. Sci. Rev.* **11**, nwae161 (2024).

[29] Liu, Y.-P. *et al.* A millisecond integrated quantum memory for photonic qubits. *Sci. Adv.* **11**, eadu5264 (2025).

[30] Ma, Y. *et al.* A Raman heterodyne study of the hyperfine interaction of the optically-excited state ⁵D₀ of Eu³⁺:Y₂SiO₅. *Journal of Luminescence* **202**, 32–37 (2018).

[31] Lauritzen, B. *et al.* Spectroscopic investigations of Eu³⁺:Y₂SiO₅ for quantum memory applications. *Phys. Rev. B* **85**, 115111 (2012).

[32] Roos, I. & Mølmer, K. Quantum computing with an inhomogeneously broadened ensemble of ions: Suppression of errors from detuning variations by specially adapted pulses and coherent population trapping. *Phys. Rev. A* **69**, 022321 (2004).

[33] Pascual-Winter, M. F., Tongning, R.-C., Chanelière, T. & Gouët, J.-L. L. Securing coherence rephasing with a pair of adiabatic rapid passages. *New J. Phys.* **15**, 055024 (2013).

[34] Gündoğan, M., Ledingham, P. M., Kutluer, K., Mazzera, M. & de Riedmatten, H. Solid state spin-wave quantum memory for time-bin qubits. *Phys. Rev. Lett.* **114**, 230501 (2015).

[35] Specht, H. P. *et al.* A single-atom quantum memory. *Nature* **473**, 190–193 (2011).

[36] Massar, S. & Popescu, S. Optimal extraction of information from finite quantum ensembles. *Phys. Rev. Lett.* **74**, 1259–1263 (1995).

Acknowledgments: This work is supported by the Quantum Science and Technology-National Science and Technology Major Project (No. 2021ZD0301200) the National Natural Science Foundation of China (Nos. 12222411 and 11821404). Z.-Q.Z acknowledges the support from the Youth Innovation Promotion Association CAS.

Author contributions: Z.-Q.Z. designed the experiment and supervised all aspects of this work; Y.-C.L. performed the experiment and analyzed the data with the help from Y.-J.Z.; Y.-C.L. and Z.-Q.Z. wrote the manuscript; Z.-Q.Z. and C.-F.L. supervised the project. All authors discussed the experimental procedures and results.

Competing interests: The authors declare that they have no competing interests.

Data and materials availability: All data needed to evaluate the conclusions in the article are present in the paper or the supplementary materials.